On the Performance of the Range Imaging Technique Estimated Using Unmanned Aerial Vehicles During the ShUREX 2015 Campaign

Hubert Luce, Hiroyuki Hashiguchi, Lakshmi Kantha, Dale Lawrence, Toshitaka Tsuda, Tyler Mixa, Masanori Yabuki

On the Performance of the Range Imaging Technique Estimated Using Unmanned Aerial Vehicles During the ShUREX 2015 Campaign

Hubert Luce, Hiroyuki Hashiguchi, Lakshmi Kantha, Dale A. Lawrence, Toshitaka Tsuda, Tyler Mixa, and Masanori Yabuki

***Abstract*— For the first time, the performance of the range imaging technique of the very high frequency band middle and upper atmosphere (MU) radar (Shigaraki observatory, Japan), when using frequency diversity, is assessed. This is done by the detection of unmanned aerial vehicles (UAVs) operated near the radar during the Shigaraki UAV radar experiment campaign, carried out from June 1, 2015 to June 14, 2015. During this campaign devoted to the measurements of fine-scale turbulence and stability in the lower troposphere using the turbulence sensors on the DataHawk UAV and the MU radar, the detection of the small UAV by the MU radar provided an excellent opportunity for taking stock of the range imaging technique in the presence of a single hard target. It was found that range imaging reproduces a faithful image of the aircraft position and its displacements with an excellent accuracy (of the order of ∼10 m), giving extra credence to the thin echo layers and their vertical displacements generally observed from the range imaging technique in stably stratified conditions.**

***Index Terms*— Adaptive filters, atmospheric measurements, geoscience and remote sensing, instrumentation and measurements, radar imaging, radar interferometry, radar measurements, signal processing.**

I. Introduction

DURING a 15-day campaign called "Shigaraki Unmanned Aerial Vehicle (UAV) Radar EXperiment" (ShUREX) carried out from June 1, 2015 to June 14, 2015 at Shigaraki middle and upper atmosphere (MU) observatory (Japan), small, lightweight, low-cost, autonomous UAVs were operated in the very close vicinity of the MU radar (see [7]). Very nearly collocated *in situ* measurements of temperature, humidity, pressure, and winds, and high-resolution measurements of turbulence, such as temperature turbulence structure function parameters and turbulent energy dissipation rates, were made using turbulence sensors carried by the UAV.

Manuscript received January 4, 2017; revised May 9, 2017 and July 6, 2017; accepted October 18, 2017. *(Corresponding author: Hubert Luce.)*

H. Luce is with the Mediterranean Institute of Oceanography, Université de Toulon, CNRS/INSU, IRD, 13288 Marseille, France (e-mail: luce@univ-tln.fr).

H. Hashiguchi, T. Tsuda, and M. Yabuki are with the Research Institute for Sustainable Humanosphere, Kyoto University, Kyoto 611-0011, Japan.

L. Kantha, D. A. Lawrence, and T. Mixa are with the Department of Aerospace Engineering Sciences, University of Colorado Boulder, CO 80309 USA.

Color versions of one or more of the figures in this paper are available online at http://ieeexplore.ieee.org.

Digital Object Identifier 10.1109/TGRS.2017.2772351

The context, goals, and some preliminary results of the ShUREX campaign are described in detail in [7]. Other results with the same UAVs obtained at the Jicamarca Radio Observatory (Peru) were shown in [15]. In this paper, as an aside to the main objectives of the campaign, we focused on detection of the UAV by the very high frequency band MU radar. Indeed, the radar cross section of the UAV was enough for detection by the radar, mainly from side lobes, without receiver saturation. The MU radar was operated continuously in range imaging mode, using five closely spaced carrier frequencies (see [10], [11]) at vertical incidence. During one of the flights, the DataHawk was commanded to fly a series of almost constant altitude circles around the center of the MU radar antenna, and on one occasion crossed the center of the main lobe oriented vertically. The configuration of the aircraft flight was suitable for validating the expected performance of the range imaging mode. Earlier comparisons from balloon data and Raman lidar data had permitted evaluation of the performance of the range imaging technique in terms of range resolution improvements [12], [13], but it is the first time that it is made from a known target with controlled positions. In addition, because the GPS altitude of the aircraft was precisely known, a very accurate calibration in altitude of the MU radar could also be achieved. Reference [3] used pass-by commercial aircrafts for phase calibration of dual frequency domain interferometry (FDI) technique, but the method does not provide absolute range calibration, since the absolute position of the aircrafts was unknown.

In Section II, the ShUREX campaign is described briefly, and the results are presented in Section III. In particular, echo power image obtained from the conventional five-frequency adaptive filter-bank Capon method is compared with images obtained from processing methods with two frequencies and from the parametric multiple signal classification (MUSIC) algorithm. The conclusion is given in Section IV.

II. Description of the ShUREX Campaign

A. DataHawk UAV System

The small, lightweight, and inexpensive UAV, DataHawk, was developed at the University of Colorado [9]. The wingspan of the current version is 1.5 m and its mass is 1.1 kg. It carries high-resolution (0.1 kHz) pitot tube and cold wire sensors. It is propelled by a pusher prop in the rear powered by an electric motor running on a 11-V, 7.6-Ah LiPo battery pack.

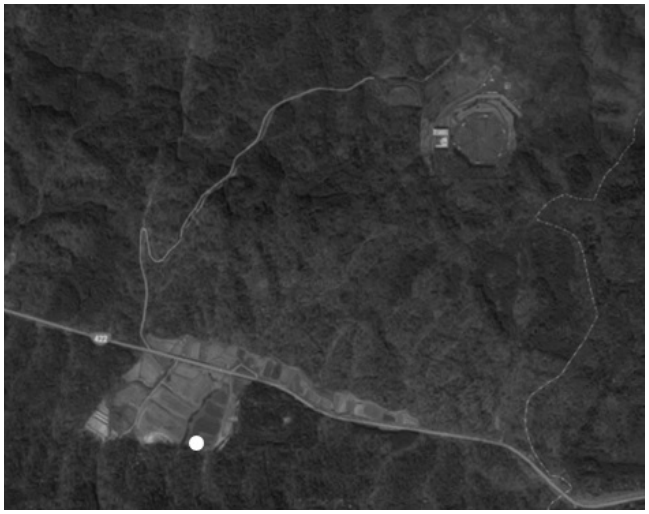

Fig. 1. Satellite map of the MU radar antenna array located at 34.854 061° N, 136.105 606° E, 378 m ASL, and UAV launching site indicated by a filled white circle (34.848 332 8° N, 136.097 497 6 E). The launching site was located at about 1-km southwest of the radar antenna array.

It can be bungee or balloon launched and has an endurance of 60–90 min depending on the climb rate. Airspeed ranges from 10 to 25 $m \cdot s^{-1}$. It has a custom-designed autopilot, which keeps the UAV on its preplanned trajectory from launch to recovery, and operators need to only supervise the flight, changing trajectory parameters, but need not fly the aircraft itself. However, the UAV can also be commanded by the operator in real time to sample a nearby atmospheric structure as indicated by, say, the radar images. The range is limited to around 20–40 km, determined by the uplink/downlink antenna gain and for safety (communication with the operator). DataHawk is well suited to making atmospheric measurements up to altitudes of 4 (bungee launch) and 7 km (balloon launch). It uses GPS for navigation. The design of the DataHawk, the characteristics of ground support components, and some data collected from these systems are described in [1], [7], [9], and [15].

The UAV launch site was situated roughly 1 km southwest of the MU radar antenna (Fig. 1) on the edge of a fallow field. This site was selected for its proximity to the MU radar site and because it was sufficiently broad for secure takeoffs and landings in a mountainous and forest terrain. The takeoffs were mainly by a bungee launch (see [7] for more details). GPS information at 1 Hz and data about flight conditions were received in real time by a ground-based receiver so that the aircraft could be monitored and commanded in real time to sample interesting atmospheric structures. Therefore, the GPS position of the aircraft was known every second.

Because wind speeds smaller than 12–16 $m \cdot s^{-1}$ [9] were required in the present experimental conditions along the trajectory of the aircraft for optimally controlled flights, MU radar data were processed almost in real time for estimating wind speed and shear profiles. The UAV was operated when the radar-derived winds were weak enough during the flight. The wind estimates were found to be sufficiently accurate for that purpose and were generally consistent with the winds encountered by the aircraft.

B. MU Radar Data

The MU radar is a Doppler pulsed radar operating at 46.5 MHz (6.45-m radar wavelength, 3.5-MHz bandwidth, and 1-MW peak output power) (e.g., [18]). It is located at 34.854 061° N, 136.105 606° E, 378 m above sea level (ASL). During the campaign, it was operated in range imaging mode (called FII in [10]) at vertical incidence using five closely spaced frequencies (46, 46.25, 46.50, 46.75, and 47 MHz), switched pulse to pulse. Because the radar controller system imposes that the number of beams must be a multiple of the frequency number used, a total of ten beam directions were programmed: five beams along the zenith at the five frequencies (for range imaging along the vertical direction only) and five beams steered 10° off zenith toward N (at 46 MHz), NE (at 46.25 MHz), E (at 46.50 MHz), SE (at 46.75 MHz), and S (at 47 MHz), respectively. These oblique beams were included for estimating horizontal winds and for analyzing the horizontal homogeneity of the atmospheric parameters. With the radar parameters used, a period of 16.384 s was necessary for collecting a time series of 128 points for all ten beam directions. A Hanning weighting window was applied to the time series before applying a fast Fourier transform so that an effective acquisition time was $\sim 16.384/2 = 8.192$ s. Profiles of parameters (echo power, velocity, spectral width, etc.) were obtained every 4.096 s by applying a time oversampling of a factor 4 for a better time continuity between the profiles. The radar transmission was stopped every 32 min for about 1 min for technical reasons.

A 16-bit optimal complementary code was applied for the transmitted pulse, as routinely used with the MU radar. Because the present results are an aside of the ShUREX campaign objectives, the effects of the choice of pulse coding on the present results were not considered when doing the experiment. The subpulse duration τ was 1μs, corresponding to a range resolution of 150 m before the application of the range imaging technique. When processing radar data in the range imaging mode, the vertical sampling was arbitrarily set to 5 m for the nominal altitudes of 1.245–20.445 km ASL. The reader is referred to [10] or [14] for the basics of the range imaging technique. The necessary information about data processing is briefly recalled in the Appendix.

The filter-bank Capon processing method is now widely used (see [4]–[6], [17]), since it does not require any information about the distribution of the targets and is not based on any model of sources. Therefore, it is expected that the Capon image represents a faithful image of the distribution of targets to which the radar is sensitive, with limitations inherent in the resolution performance of the method according to the signal-to-noise ratio (SNR). The effects of the number of frequencies and SNR on the performance are theoretically well known (see [10]) but they are experimentally described in this paper. In addition, the MUSIC algorithm, based on the singular-value decomposition of the covariance matrix of the received signals, is applied. It is a parametric method assuming a known number of fixed and discrete targets or sources (in its most widespread form, see [2]). It is not adapted to distributed atmospheric scatterers (see [10]), but under certain conditions,

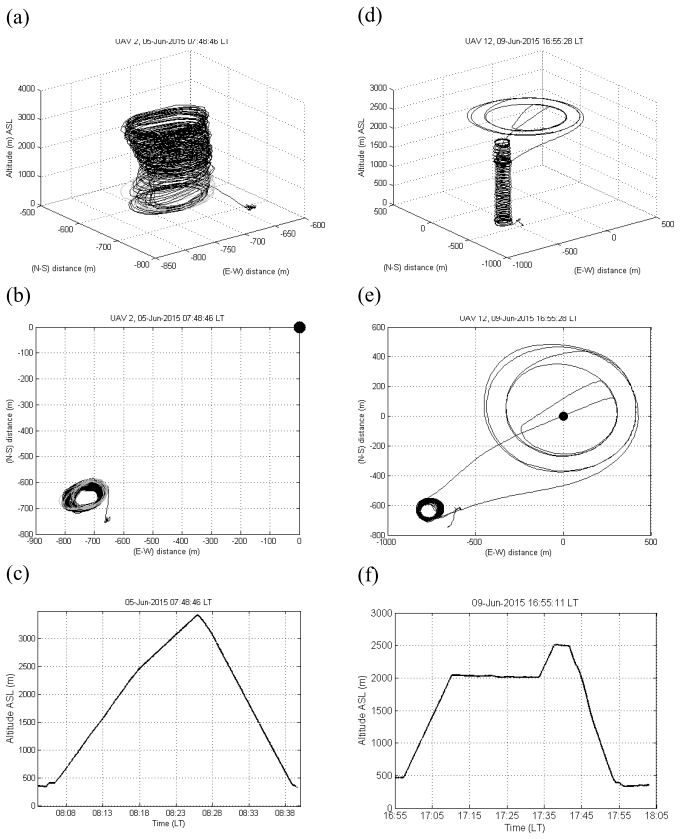

Fig. 2. (a) Plot of trajectory of UAV2 during the 50-min flight on June 5, 2015 from 07:48 LT. (b) Plot of GPS (E–W) distance versus (N–S) distance from the MU radar. Black curve shows the data during the ascent (up to 3425 m ASL), and gray curve shows the data during the descent. (c) Height versus time plot for the UAV flight. (d) Plot of trajectory during the 68-min UAV12 flight on June 9, 2015 from 16:55 LT. (e) Plot of GPS (E–W) distance versus (N–S) distance from the MU radar for the 68-min UAV flight. (f) Height versus time plot for the 68-min UAV flight. In (b) and (e), the black dot indicates the position of the MU radar antenna array.

it can be used for the detection of the UAV as we shall see in Section III-A.

III. Results

A. Selected UAV Trajectories

Fig. 2 shows information on the trajectories of two aircraft flights made on June 5 from 07:42 LT (UAV2) and June 9 from 16:55 LT (UAV12), respectively. On June 5, the aircraft ascended from the ground up to 3425 m ASL at a vertical velocity of $\sim$2.5 m·s^{-1} and then descended back to the ground at $\sim$3.9 m·s^{-1} [Fig. 2(c)]. The aircraft was climbing and descending along a helical trajectory of an almost constant diameter of 100 m [Fig. 2(a) and (b)]. Fig. 2(d)–(f) shows the corresponding data for the aircraft flight on June 9. The aircraft first ascended near the launching site in a helical pattern of $\sim$120 m in diameter from the ground up to $\sim$2040 m ASL at a vertical velocity of 2 m·s^{-1} for $\sim$13 min. Then, the aircraft was directed toward the MU radar antenna and was flying a series of constant height circles at two slightly different levels centered on the MU radar antenna. During this period, the aircraft first made two and a half circles of $\sim$850 m in diameter at $\sim$2033 m ASL for about 11 min from $\sim$17:11 LT and then made two circles of $\sim$620 m in diameter at $\sim$2015 m ASL for about 4.5 min. After these sequences, the aircraft passed near the vertical axis of the radar antenna around 17:26 LT and exactly over the vertical around 17:28 LT. It went back toward the launching site and made a series of additional helical patterns of $\sim$120 m in diameter before descending to the ground. A detailed description of the UAV12 flight is given in Table I. The flight is divided into sequences called S1, S2, etc., for easy reference when comparing with radar data.

The trajectory of the aircraft between 17:11 and 17:30 LT on June 09 (sequences S3–S7 in Table I) is particularly interesting for our purpose, because it was flying almost at a constant distance with respect to the radar antenna so that the radial velocity of the aircraft (i.e., the velocity component parallel to line of sight of the radar beam) was minimized. It was not exactly zero because the center of the circles did not fully coincide with the center of the radar antenna [Fig. 2(e)]. To some extent, the vehicle could be considered as a "fixed and discrete target" at a known distance from the radar antenna when flying along a circular pattern with constant diameter and center on the radar antenna. Conditions were then good for evaluating the performance of the range imaging technique using the Capon method or MUSIC algorithm and for an accurate calibration in distance of the MU radar.

The radii of the circles and the altitudes of flight were initially chosen so that the aircraft was flying into theoretical nulls of the radar antenna beam pattern. However, signals backscattered from the aircraft were always detected and the receiver did not saturate even when the aircraft was illuminated by the main beam.

B. MU Radar Echo Power Image in Capon Range Imaging Mode

Fig. 3(a) shows the time–height cross section of radar echo power at vertical incidence P_{MU} (dB, in arbitrary level) after performing the conventional Capon processing described in Section III-A, from 07:30 to 09:30 LT on June 5, 2015, up to the altitude of 6.5 km ASL, and surrounding the UAV flight described in Fig. 2(a)–(c). The radar plots in this paper have already included the small altitude correction obtained from comparisons with the UAV position (as described later). The echo produced by the UAV flying from 07:48 LT appears clearly as a thin triangular-shaped line from 08:08 until 08:35 LT, below a deep turbulent layer developing from $\sim$08:10 LT at the altitude of $\sim$5 km. The time evolution of the UAV echo reminds us of the height–time curve of Fig. 2(c), but its position corresponds to its distance from the radar [+378 m for the conversion above the ground level (AGL) to ASL], not its altitude.

Fig. 3(b) shows similar information as Fig. 3(a) from 16:30 to 18:00 LT on June 9, 2015, surrounding the UAV flight described in Fig. 2(d)–(f). The signature of the UAV is more difficult to distinguish from 17:00 to 17:50 LT, due to stronger atmospheric echoes showing clear wavy patterns. These wavy patterns clearly coincide with, and are likely due to the presence of a deep turbulent layer in the height range 4–6 km. (The interpretation of these features is beyond the scope of this paper but presented elsewhere.)

TABLE I

MAIN CHARACTERISTICS OF THE UAV12 FLIGHT. *: GIVEN WITH RESPECT TO THE SEA LEVEL (ASL), i.e., +378 m AGL. **: GEOMETRICAL DISTANCE BETWEEN THE UAV LOCATION AND THE CENTER OF THE RADAR ANTENNA

Sequence number	Start-End time (LT)	Duration (s)	Altitude range (m)*	Distance (m)**	Mode
S1	16:55:11 17:10:17	906	472-2041	918-1970	Helical pattern (diameter ~120 m, center: (-760m,-620m) from MU radar antenna)
S2	17:10:18 17:11:18	60	2040-2041	1966-1718	Near straight line toward MU radar
S3	17:11:19 17:21:55	636	2041-2024	1717-1706	Circular pattern (diameter ~850 m) Center: MU radar antenna
S4	17:21:56 17:26:32	276	2024-2018	1706-1670	Circular pattern (diameter ~620 m) Center: MU radar antenna
S5	17:26:33 17:27:20	47	2018-2011	1669-1652	Straight line (above MU radar antenna)
S6	17:27:21 17:28:16	55	2011-2008	1654-1657	Half a circle (diameter ~620 m) Center: MU radar antenna
S7	17:28:17 17:30:15	118	2008-2012	1656-1901	Nearly straight line (passed over the center of MU radar antenna at 17:29 LT)
S8	17:30:16 17:33:43	207	2012-2012	1907-1915	Circular pattern (diameter ~120 m, center: (-760m,-620m) from MU radar antenna)
S9	17:33:44 17:38:01	257	2013-2509	1921-2342	Helical pattern (diameter ~120 m, center: (-760m,-620m) from MU radar antenna)
S10	17:38:02 17:41:49	227	2509-2487	2345-2317	Circular pattern (diameter ~120 m, center: (-760m,-620m) from MU radar antenna)
S11	17:41:50 17:55:22	812	2485-384	2319-1044	Helical pattern (diameter ~120 m, center: (-760m,-620m) from MU radar antenna)

Because the flight conditions on June 9 [Fig. 3(b)] were the most adapted to the purpose of this paper, we only focus on the 32-min radar sequence collected from 17:04 LT during which the UAV was flying around the center of the MU radar antenna. A close-up of Fig. 3(b) is shown in Fig. 4(a), along with the corresponding sequences S1–S9 of UAV flight (see Table I). The signature of the UAV in the Capon image reveals not only the variations of height shown in Fig. 2(e) but also the variations of distance due to the helical trajectory of the aircraft (as suggested by short-time periodic oscillations of the echoes during S1 and S8). The black spots during S5 and S7 just above 2 km correspond to the passage of the UAV inside the main lobe. The echoes were thus the strongest at those times. At 17:29 LT (S7), the altitude of the UAV was equal to the distance from the antenna.

C. Results From Alternative Processing Methods

Because this paper addresses the range imaging technique performances, additional results from other processing methods are presented. They are devoted to convince the reader about the relevance of the conventional Capon method on pulsed radars.

In addition to the five-frequency Capon processing shown in Fig. 4(a), the other panels of Fig. 4 show (for the same period and the same height range) the following.

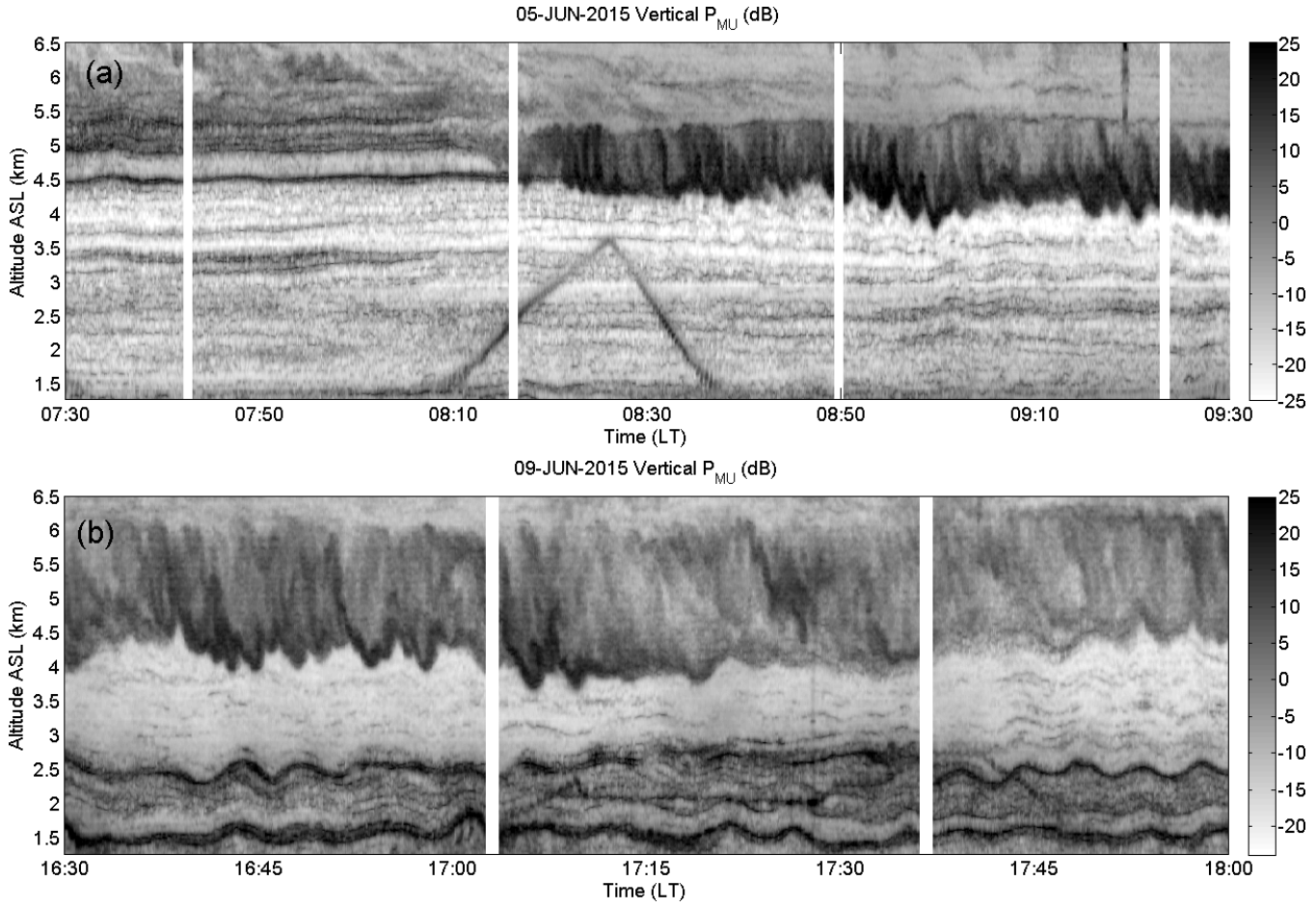

Fig. 3. (a) Time–height cross section of echo power P_{MU} (dB) at vertical incidence after performing the Capon processing in the height range 1.27–6.5 km from 07:30 to 09:30 LT on June 5, 2015. (b) Time–height cross section of echo power P_{MU} (dB) at vertical incidence after performing the Capon processing in the height range 1.27–6.5 km from 16:30 to 18:00 LT on June 9, 2015.

1) The corresponding time–height cross section of SNR at the range resolution of 150 m defined by the subpulsewidth, 1 μs [Fig. 4(b)].
2) Two images after performing the Capon processing method with two frequencies only for the maximum frequency spacing ($\Delta f_{\max} = 1$ MHz) [Fig. 4(c)] and for $\Delta f = 0.25$ MHz (i.e., the frequency separation used when five equally spaced frequencies are used) [Fig. 4(d)].
3) An image after performing the dual-FDI technique (e.g., [19]) with $\Delta f_{\max} = 1$ MHz [Fig. 4(e)]. Nowadays, this technique is not used anymore but was recognized as a significant advance in the 1990s (e.g., [21]) before the emergence of multifrequency and coherent imaging techniques. The method is based on the estimate of the complex coherence between the signals at the two frequencies and consists of retrieving the depth and position of a single backscattering layer assumed to be embedded within each radar gate. The details of the technique and hypotheses and calculations can be found in [20] for example. The image consists of rectangles of vertical extent equal to twice the standard deviation of the Gaussian function describing the vertical distribution of the backscattering layer.
4) An image obtained from the MUSIC algorithm assuming a single source (consistent with the objective of UAV detection) [Fig. 4(f)].

The following appear clearly.

1) As expected, the observations at a resolution of 150 m cannot be used for monitoring the position of the UAV with an accuracy better than 150 m [Fig. 4(b)]. The UAV cannot even be identified during its climbing (S1). This underlines the usefulness of range imaging techniques (see [4], [6], [11]).
2) The Capon image obtained with two frequencies $\Delta f_{\max} = 1/\tau = 1$ MHz shows a similar signature of the UAV but also atmospheric peak repetition into adjacent range gates at some occasions [Fig. 4(c)]. This problem is inherent to both the presence of ambiguity lobes of the Capon filter at range intervals equal to the range resolution and overlapping of the edges of the radar weighting function at successive gates. It preferably occurs when a single target is dominant into adjacent gates [e.g., above ~2.5 km in Fig. 4(c)]. There is mostly no replica of the UAV echo, likely because the target is localized and atmospheric echoes are dominant in neighboring gates. Three UAV peaks appear into three consecutive range gates during S5, S6, and S7, because

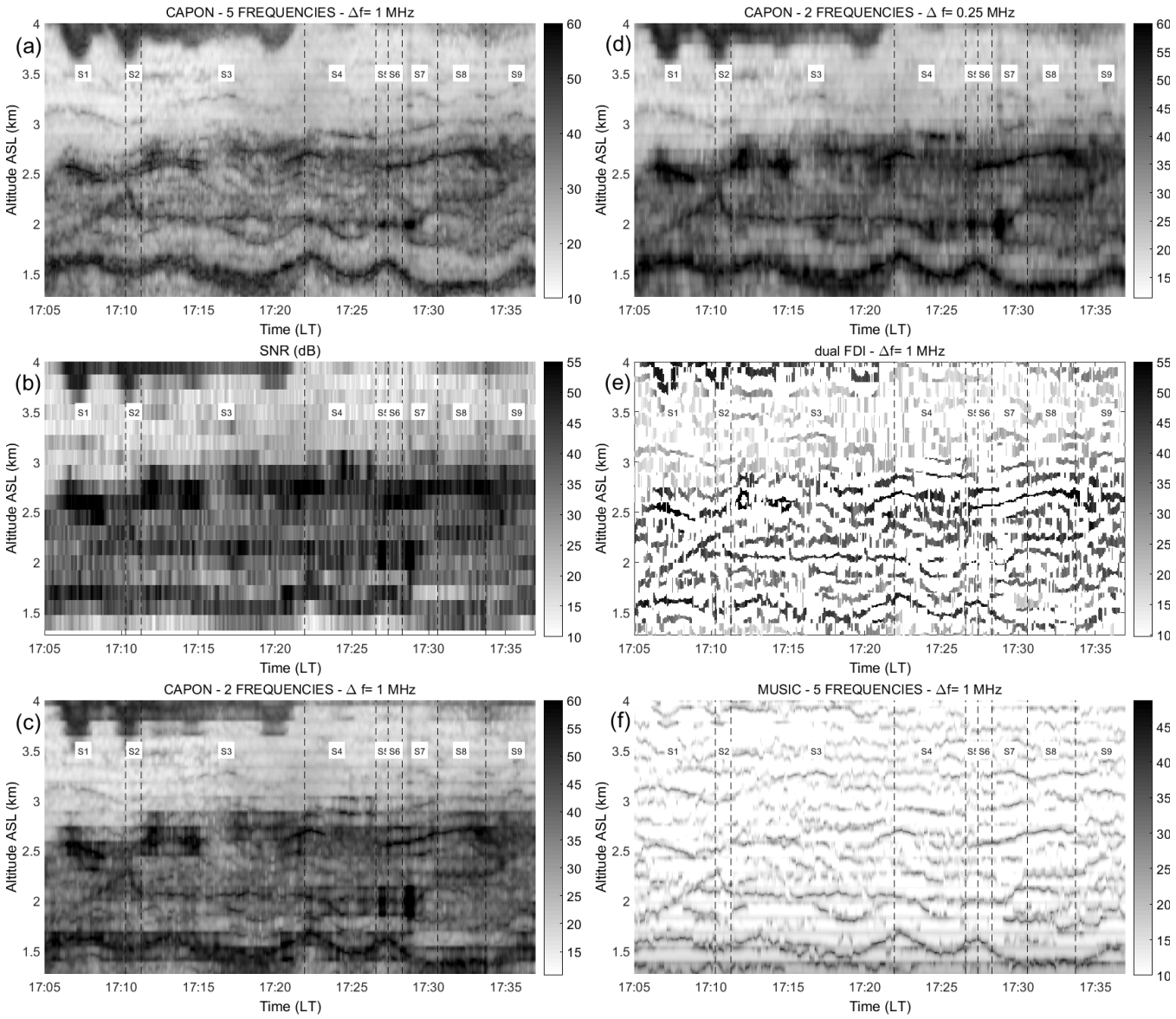

Fig. 4. (a) Zoomed-in view of Fig. 3(b) from 17:05 LT. The dashed lines delimit the sequences of flight S1–S9. (b) Time–height cross section of SNR at the range resolution of 150 m. The corresponding image obtained from the Capon processing method with two frequencies and a frequency separation of (c) 1 and (d) 0.25 MHz. (e) Image obtained from the dual-FDI technique. (f) Image obtained after applying the MUSIC algorithm (assuming a single target).

signals backscattered by the UAV were very strong when crossing the main radar lobe.

3) The Capon image obtained with two frequencies $\Delta f = 0.25$ MHz $= \Delta f_{\max}/4$ [Fig. 4(d)] reveals features that are very close to the conventional five-frequency Capon processing because the ambiguity lobes are now displaced to radar gates N±4 when the processing is performed at gate N. This configuration permits us to avoid peak replicas ("ghost" echoes) but is less robust because only two frequencies are used and the resolution is strongly degraded with respect to the conventional Capon processing (since the resolution mainly depends on the maximum frequency spacing). In particular, the UAV echo appears deeper in Fig. 4(d).
4) The image obtained from the dual-FDI technique [Fig. 4(e)] provides reasonable information when the UAV was flying at constant altitude (S3) but often failed (e.g., S2) due to its limited performance and drastic hypotheses.
5) The MUSIC image [Fig. 4(f)] shows sharp peaks for all radar gates and times, some of them being very consistent with the time evolution of maxima produced by the Capon processing (i.e., around 1.5 km and just above 3 km until 17:17 LT), some others being "artifacts" of the method [around the top right of Fig. 4(f)]. The signature of the UAV appears even more prominently than that in the Capon image so that the position of the UAV can also be easily tracked.

As a result, among the methods used, the conventional multifrequency Capon processing method appears to be the most adapted for producing high-resolution echo power images of atmospheric targets. The images of the UAV obtained

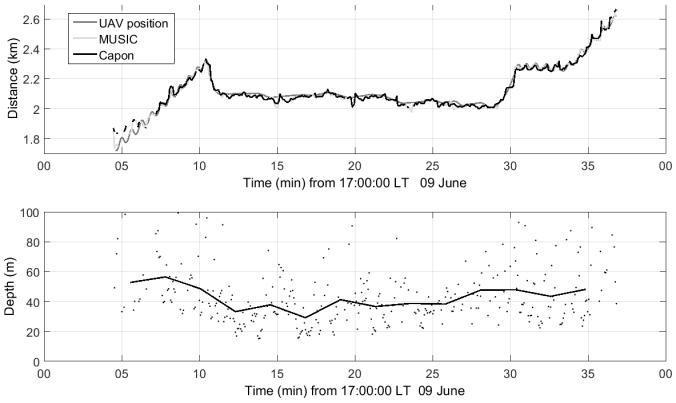

Fig. 5. (Top) Distance of the UAV launched at 17:48 LT from the radar antenna versus time (heavy gray curve) and position of the Capon and MUSIC peaks (black and light gray curves, respectively) versus time. (Bottom) Width of the Capon peak defined as twice the standard deviation of the Gaussian curve fitting the Capon peaks. Solid curve shows the averaged value over 5 min.

from alternative and/or degraded methods are not often flawed because the UAV constitutes a single and nearly discrete (unless moving) target, which is the least challenging problem of imaging techniques.

D. Comparison Between Ranges of the UAV

For a more thorough comparison between the distances of the UAV derived from the radar data in range imaging mode using the conventional Capon method and MUSIC algorithm and those provided by the GPS data, the Capon and MUSIC peaks associated with the UAV signal have been manually selected within each 4.096-s profile from 17:04:28 LT. For the Capon profiles, the detection was accompanied by a Gaussian fitting of the peaks (using seven points around the maximum). The standard deviation of the Gaussian curve defines the half width of the peak, and then the apparent size of the UAV provided by the Capon method during the acquisition period of the time series.

Fig. 5(a) shows the positions of the UAV versus time (heavy gray curve) at a time resolution of 1 s and the corresponding positions of the Capon and MUSIC peaks (black and gray curves, respectively). Conclusions to be drawn from this plot are as follows.

1) The Capon and MUSIC positions are extremely similar: the mean difference is less than 1.7 m for the whole period. Part of this difference can be from the manual selection of the peaks and is likely not meaningful. In particular, the large differences around $t = 5$ min are mainly due to a poor detection of the UAV peaks at this altitude range and the manual selection may have been wrong if the atmospheric signals merged with UAV signals. Therefore, the Capon and MUSIC methods provide information on target positions, which are fully consistent with each other.
2) The correspondence between the GPS positions and the radar-derived positions is excellent after a small (and already applied) correction of +25 m of the radar altitudes with respect to the nominal altitudes. This offset corresponds to the altitude difference between the GPS position of the aircraft and the positions of its peak in the Capon and MUSIC images (found to be identical) at 17:29 LT, when the aircraft passed over the center of the radar antenna within a few meters (so that distance is equal to the altitude). This analysis thus permitted the most accurate altitude calibration of the MU radar to be obtained so far. Because the GPS altitude can sometimes be faulty, a calibration from a single flight may not be reliable. However, we also obtained very consistent results from comparisons with 11 additional flights during the campaign, after applying the altitude correction (not shown), indicating that the GPS data were relevant during the flight used for the present studies.
3) After altitude correction, a small difference of −9.5 m in average still remains during S3 and S4, when the aircraft made circular patterns around the MU radar antenna. "Contamination" by atmospheric echoes can be the main source of bias, when estimating the characteristics of the UAV peaks. In the present case, an atmospheric echo showing wavelike disturbances can be seen just below the altitude of the UAV echo at 13 and 23 min during S3 and S4 [Fig. 4(a)] so that the UAV distance might be slightly underestimated. Therefore, it is better not to consider the sequences S3 and S4 for an accurate altitude calibration.
4) The variations of distance of the UAV when making helical or circular patterns during S1 and S8 are detected by both the Capon and MUSIC methods. During S8, the amplitude of the GPS distance oscillations was ∼60 m. The corresponding time variation of positions of the Capon or MUSIC peaks was 30–40 m, in close agreement with the real displacements, despite smoothing effects due to the time resolution of the radar.

Fig. 5(b) shows the corresponding width of the Capon peaks. The smallest values are observed from S3 to S6 (17:11 to 17:28 LT), when the aircraft was flying around the MU radar antenna (so that its distance was nearly constant). During the other sequences, the radial displacements of the aircraft were more important so that the UAV was a moving target, implying wider peaks. The mean width value was 36 m between S3 and S6, with minimum values of about 20 m. It is in reasonable agreement with the expected performances of the Capon method for high SNR. From numerical simulations performed in [10], the apparent width of a discrete targets should be of the order of 10 m for SNR larger than 15 dB (as is the case here, not shown). The difference can be explained by the small but nonnegligible displacements of the aircraft [the trajectory of the aircraft was not exactly transverse to the radar beam pattern, see Fig. 2(e)]. In addition, the presence of atmospheric echoes can also be a source of bias. For example, around 17:15 LT, an atmospheric echo merged with the aircraft echo, resulting in an increase of the width of the peak up to about 60 m. An atmospheric echo also merged with aircraft echo after 17:21:56 LT (S4) when the UAV was flying toward the radar for reducing the diameter of the circular pattern around the MU radar antenna. Despite of these conditions, the width of the UAV peaks did not increase, perhaps due to

the complexity of the high-resolution patterns and arbitrary manual selection.

IV. Conclusion

The ShUREX 2015 campaign was carried out at the Shigaraki MU observatory for comparing the MU radar data with data collected by the Datahawk UAV within the lower troposphere. In this paper, as an aside to the main goals of the campaign described in [7], we analyzed the performance of the range imaging technique, using the aircraft signal in the high-resolution, height–time cross sections of radar echo power. Even though the range imaging technique with the Capon processing method has proven its worth for more than ten years with the MU radar, it is the first time that the performance of the technique was assessed from an identified (and almost discrete) target at known distances. These studies come very late after the development of the technique itself, but UAVs were not available until recently and, therefore, it was not possible to make such comparisons before.

It was found that the conventional Capon processing provides a faithful image of the target (in particular, with no "ghost" echo), as well as an estimate of its position, with an excellent accuracy and small distance variations (of the order of a few tens of meters or less), which could be monitored in the conditions of the present experiments. Such an accuracy cannot be obtained in a standard mode, even with a short pulse radar such as the SOUSY radar (pulselength of 0.25 μs and range resolution of 37.5 m, [16]). The degraded versions of range imaging using two frequencies and the dual-FDI technique show drawbacks that are consistent with the theoretical expectations and, therefore, should not be used for operational purposes. The MUSIC algorithm, which is well adapted to the detection of a discrete target, fully confirms the positions provided by the Capon method. Therefore, there is no estimation bias specific to the Capon method. In addition, the width of the aircraft echoes (down to ~20 m, when it was flying around the MU radar) was in reasonable agreement with what we can expect from the Capon performance for a discrete source. It is thus the typical accuracy that we can expect from the Capon method for high SNR.

The use of a single target does not permit us to evaluate the practical performance of the technique for separating several targets. It is a major issue that is not addressed in this paper. The main purpose of this paper was to demonstrate the relevance of the technique for detecting the position and displacements of a target without the generation of ghost echoes due to some ambiguity lobes and with an accuracy that cannot be achieved by a simple reduction of the pulsewidth. In addition, the Capon method not only reveals fine structures, but can also highlight deep turbulent layers, such as those reported in Fig. 3. The range imaging technique is thus definitely a reliable technique for improving the precision of pulse radars, even if the results obtained with a small and hard target may not provide quantitative information on the performance that would be obtained from atmospheric targets.

Finally, the ShUREX campaign provided an excellent opportunity for a very accurate height calibration of the MU radar in standard (i.e., one frequency) mode and for the range imaging mode configuration used during the campaign (within ~10 m or so). An absolute calibration in range imaging mode requires a phase calibration depending on some radar parameters used (frequencies, pulse shape and width, pulse coding, etc.) [5] so that another calibration would be necessary for another range imaging mode configuration.

Appendix
Capon Processing and MUSIC Algorithm

We very briefly recall the fundamentals of the radar backscattered signal processing methods. The reader may refer to a more specialized literature for additional information.

The transmitter frequency is varied pulse to pulse so that N signals at N closely spaced frequencies are collected. The complex time series for frequency i $(1 \leq i \leq N)$ is denoted as $s_i(t)$.

A. Capon Method

A filter-bank processing method consists in calculating a weighted average of these time series

$$\boldsymbol{y}(t) = \boldsymbol{h}^{\dagger}(r) \cdot \boldsymbol{s}(t)$$

where the dagger represents the Hermitian operator and

$$\boldsymbol{s}(t) = [s_1(t) \ \ldots s_i(t) \ \ldots s_N(t)]^T.$$

The complex weighting vector is determined according to optimal conditions. If the linear filter given by h passes the signals without phase distortion and no attenuation at the desired range r and minimizes an output variance or power in ranges different from the desired r as much as possible, the optimal Capon processing filter is obtained. It is found that

$$\mathbf{h}(r0) = \frac{\boldsymbol{R}^{-1}\mathbf{a}(r)}{\mathbf{a}^{\dagger}(r)\boldsymbol{R}^{-1}\boldsymbol{a}(r)}$$

where $\boldsymbol{R} = \langle \mathbf{s}(t)\mathbf{s}^{*}(t) \rangle$ is the covariance matrix of $\mathbf{s}(t)$ and $\mathbf{a}(r) = [1 \ \ldots \exp \ (-2jkr) \ldots \ \exp(-2j(N-1)\Delta kr)]^{\mathrm{T}}$ is the steering vector for equally spaced frequencies. k is the wavenumber difference between two consecutive frequencies

$$P_c(r) = \langle \mathbf{y}(t)\mathbf{y}^{\dagger}(t) \rangle = (\mathbf{a}^{\dagger}(r)\boldsymbol{R}^{-1}\boldsymbol{a}(r))^{-1}.$$

B. MUSIC Algorithm

The eigensystem approach introduced in [2] uses a decomposition of $\boldsymbol{R}$ in singular values. The N-dimensional space is decomposed into two orthogonal vector spaces: the signal and the noise vector subspaces of dimensions M and $(N-M)$, respectively. M is the number of discrete sources, either known or assumed. Let us consider $\mathbf{T} = [\boldsymbol{t_1} \ \ldots \ \boldsymbol{t_{N\text{-}M}}]$ as the matrix of eigenvectors associated with the noise subspace. Because the signal subspace is orthogonal to the noise subspace, then

$$\boldsymbol{a}^{\dagger}(r).\boldsymbol{T} = 0.$$

The MUSIC algorithm provides a pseudo-distribution

$$P_M(r) = (\mathbf{a}^{\dagger}(r)\boldsymbol{T}\boldsymbol{T}^{\dagger}\boldsymbol{a}(r))^{-1}.$$

For the purpose of this paper, we put $M = 1$.

Acknowledgment

The authors would like to thank JSPS for providing partial funding for the ShUREX campaign.

REFERENCES

[1] B. B. Balsley, D. A. Lawrence, R. F. Woodman, and D. C. Fritts, "Fine-scale characteristics of temperature, wind, and turbulence in the lower atmosphere (0–1,300 m) over the south peruvian coast," *Boundary-Layer Meteorol.*, vol. 147, no. 1, pp. 165–178, 2013, doi: 10.1007/s10546-012-9774-x.

[2] G. Bienvenu and L. Kopp, "Optimality of high resolution array processing using the eigensystem approach," *IEEE Trans. Acoust., Speech, Signal Process.*, vol. ASSP-31, no. 5, pp. 1235–1248, Oct. 1983.

[3] J.-S. Chen, "On the phase biases of multiple-frequency radar returns of mesosphere-stratosphere-troposphere radar," *Radio Sci.*, vol. 39, no. 5, p. RS5013, 2004, doi: 10.1029/2003RS002885.

[4] J.-S. Chen and M. Zecha, "Multiple-frequency range imaging using the OSWIN VHF radar: Phase calibration and first results," *Radio Sci.*, vol. 44, no. 1, p. RS1010, 2009, doi: 10.1029/2008RS003916.

[5] J.-S. Chen, C.-L. Su, Y.-H. Chu, G. Hassenpflug, and M. Zecha, "Extended application of a novel phase calibration approach of multiple-frequency range imaging to the Chung–Li and MU VHF Radars," *J. Atmos. Ocean. Technol.*, vol. 26, pp. 2488–2500, Nov. 2009.

[6] P. B. Chilson, R. D. Palmer, A. Muschinski, D. A. Hooper, G. Schmidt, and H. Steinhagen, "SOMARE-99: A demonstrational field campaign for ultrahigh-resolution VHF atmospheric profiling using frequency diversity," *Radio Sci.*, vol. 36, no. 4, pp. 695–707, 2001.

[7] L. Kantha *et al.*, "Shigaraki UAV-Radar Experiment (ShUREX 2015): An overview of the campaign with some preliminary results," *Prog. Earth Planetary Sci.*, vol. 4, p. 19, 2017, doi: 10.1186/s40645-017-0133-x.

[8] D. A. Lawrence, E. W. Frew, and W. J. Pisano, "Lyapunov vector fields for autonomous unmanned aircraft flight control," *AIAA J. Guid. Control. Dyn.*, vol. 31, no. 5, pp. 1220–1229, 2008.

[9] D. A. Lawrence and B. B. Balsley, "High-resolution atmospheric sensing of multiple atmospheric variables using the DataHawk small airborne measurement system," *J. Atmos. Ocean. Technol.*, vol. 30, pp. 2352–2366, Oct. 2013.

[10] H. Luce, M. Yamamoto, S. Fukao, D. Helal, and M. Crochet, "A frequency domain radar interferometric imaging (FII) technique based on high-resolution methods," *J. Atmos. Solar-Terrestrial Phys.*, vol. 63, nos. 2–3, pp. 221–234, 2001.

[11] H. Luce, G. Hassenpflug, M. Yamamoto, and S. Fukao, "High-resolution vertical imaging of the troposphere and lower stratosphere using the new MU radar system," *Ann. Geophys.*, vol. 24, pp. 791–805, May 2006.

[12] H. Luce, G. Hassenpflug, M. Yamamoto, and S. Fukao, "Comparisons of refractive index gradient and stability profiles measured by balloons and the MU radar at a high vertical resolution in the lower stratosphere," *Ann. Geophys.*, vol. 25, no. 1, pp. 47–57, 2007.

[13] H. Luce, T. Takai, T. Nakamura, M. Yamamoto, and S. Fukao, "Simultaneous observations of thin humidity gradients in the lower troposphere with a Raman lidar and the very high-frequency middle- and upper-atmosphere radar," *J. Atmos. Ocean. Technol.*, vol. 27, pp. 950–956, May 2010, doi: 10.1175/.2010JTECHA1372.1.

[14] R. D. Palmer, T.-Y. Yu, and P. B. Chilson, "Range imaging using frequency diversity," *Radio Sci.*, vol. 34, no. 6, pp. 1485–1496, Nov./Dec. 1999.

[15] D. E. Scipión, D. A. Lawrence, M. A. Milla, R. F. Woodman, D. A. Lume, and B. B. Balsley, "Simultaneous observations of structure function parameter of refractive index using a high-resolution radar and the DataHawk small airborne measurement system," *Ann Geophys.*, vol. 34, pp. 767–780, Sep. 2016.

[16] R. F. Woodman, G. Michhue, J. Röttger, and O. Castillo, "The MPI-SOUSY-VHF radar at jicamarca: High altitude-resolution capabilities," in *Proc. 11th Int. Workshop Tech. Sci. Aspects MST Radar*, Gadanki, India, 2007, p. 4.

[17] T.-Y. Yu and W. O. J. Brown, "High-resolution atmospheric profiling using combined spaced antenna and range imaging techniques," *Radio Sci.*, vol. 39, no. 1, p. RS1011, 2004, doi: 10.1029/2003RS002907.

[18] S. Fukao, T. Sato, T. Tsuda, M. Yamamoto, and M. D. Yamanaka, "MU radar—New capabilities and system calibrations," *Radio Sci.*, vol. 25, pp. 477–485, 1990.

[19] E. Kudeki and G. R. Stitt, "Frequency domain interferometry: A high resolution radar technique for studies of atmospheric turbulence," *Geophys. Res. Lett.*, vol. 14, pp. 198–201, 1987.

[20] S. J. Franke, "Pulse compression and frequency domain interferometry with a frequency-hopped MST radar," *Radio Sci.*, vol. 25, pp. 565–574, 1990.

[21] C. Kilburn, S. Fukao, and M. Yamamoto, "Extended period frequency domain interferometry observations at stratospheric and tropospheric heights," *Radio Sci.*, vol. 30, pp. 1099–1109, 1995.

Hubert Luce was born near Lille, France. He received the Ph.D. degree in atmospheric radar techniques from the University of Toulon, Toulon, France, in 1996.

He is currently an Associate Professor with the Mediterranean Institute of Oceanography, University of Toulon, Marseille, France. He was a Post-Doctoral Lavoisier Grant Fellow of the French Ministry of Foreign Affairs from 1998 to 2000 and a JSPS Fellow of Monbusho from 2000 to 2002 at the Radio Science Center for Space and Atmosphere, University of Kyoto, Kyoto, Japan, where he has been regularly collaborating with the Research Institute for Sustainable Humanosphere. His research interests include the study of the atmospheric dynamics at small scales from radar and *in situ* measurements.

Hiroyuki Hashiguchi received the Master degree in electrical engineering from the Faculty of Engineering and Design, Kyoto Institute of Technology, Kyoto, Japan, in 1990.

In 1995, he completed the second half of his doctoral program at the Department of Electrical Science and Engineering, Graduate School of Engineering, Kyoto University, Kyoto. In 1995, he became a Research Fellow PD of the Japan Society for the Promotion of Science. In 1997, he became a Research Associate with the Radio Atmospheric Science Center, Kyoto University (reorganized in 2000 as the Radio Science Center for Space and Atmosphere). In 2001, he became an Associate Professor at the same center (reorganized in 2004 as the Research Institute for Sustainable Humanosphere). His research interests include the development of atmospheric radars and research on observations using those radars.

Dr. Hashiguchi was a D.Eng. recipient of the 2006 Minister of Education Science and Technology Award and the 2008 Horiuchi Prize of the Meteorological Society of Japan. He is a member of the Meteorological Society of Japan, the Society of Geomagnetism and Earth, Planetary and Space Sciences, the American Meteorological Society, the American Geophysical Union, and the Institute of Electronics, Information and Communication Engineers, Japan.

Lakshmi Kantha is a Professor with the Department of Aerospace Sciences, University of Colorado, Boulder, CO, USA. He teaches aircraft and rocket propulsion, but conducts research on ocean- and atmosphere-related topics. He is an expert on numerical models of oceans, turbulent mixing, and wave motions. More recently, during his sabbatical at Kyoto University, Kyoto, Japan, he developed an interest in very high-frequency radars and their use in measuring turbulence and wave motions in the atmosphere. He conceived, organized, and led the Shigaraki Unmanned Aerial Vehicle Radar EXperiment (ShUREX) campaigns at the middle and upper atmosphere radar facility in Shigaraki, Japan.

Dale A. Lawrence received the B.S. degree in electrical engineering from Colorado State University, Fort Collins, CO, USA, in 1980, and the M.S. and Ph.D. degrees from Cornell University, Ithaca, NY, USA, in 1982 and 1985, respectively.

He is currently a Professor with the Smead Aerospace Engineering Sciences Department, University of Colorado, Boulder, CO, USA. He is the Principal Developer of the DataHawk UAS that has been deployed in atmospheric measurement campaigns in Utah, Alaska, Japan, and Peru. His research interests include control systems applied to a variety of applications in telerobotics, solar sail spacecraft, and unmanned aerial systems.

Toshitaka Tsuda was born in 1952. He received the Ph.D. degree from the Faculty of Engineering, Kyoto University, Kyoto, Japan.

In 1977, he started his research career with studies on the middle atmosphere dynamics, using radar observations at Kyoto University. He was involved in the design and implementation of the middle and upper atmosphere radar in Shigaraki, Japan, in 1984, and the equatorial atmosphere radar in west Sumatra, Indonesia, in 2001. He was promoted to Professor at Kyoto University in 1995, where he became the Director of the Research Institute for Sustainable Humanosphere, in 2010. He was elected as the President of Japan Geoscience Union in 2012. He retired in 2016.

Tyler Mixa received the M.Sc. degree in aerospace engineering from the University of Colorado, Boulder, CO, USA, in 2014, where he is currently pursuing the Ph.D. degree with the University of Colorado with L. Kantha and D. Fritts.

He researches high-frequency atmospheric gravity wave and fine structure interactions using direct numerical simulation modelling guided by observational data. His research interests include identifying the quantitative influences of gravity wave–fine structure interactions and determining how these dynamics manifest in mesosphere and lower thermosphere observations and the extent to which they influence similar flow environments in the rest of the atmosphere.

Masanori Yabuki received the Dr.Sc. degree from Chiba University, Chiba, Japan, in 2003.

He is currently an Assistant Professor with the Research Institute for Sustainable Humanosphere, Kyoto University, Kyoto, Japan. He is a member of the Meteorological Society of Japan, the Japan Association of Aerosol Science and Technology, the Remote Sensing Society of Japan, and the American Geophysical Union. His research interests include the observational study of aerosol–cloud optical properties and the development of lidar techniques for atmospheric measurements.